

# Digital Microarrays: Single-Molecule Readout with Interferometric Detection of Plasmonic Nanorod Labels

Derin Sevenler,<sup>\*,†</sup> George G. Daaboul,<sup>‡</sup> Fulya Ekiz Kanik,<sup>†</sup> Neşe Lortlar Ünlü,<sup>§</sup> and M. Selim Ünlü,<sup>†,§</sup>

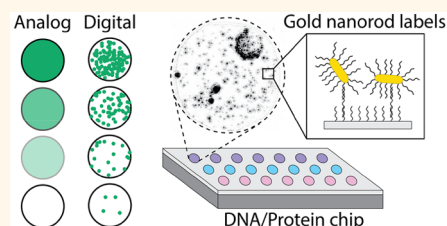
<sup>†</sup>Department of Electrical and Computer Engineering and <sup>§</sup>Department of Biomedical Engineering, Boston University, Boston, Massachusetts 02215, United States

<sup>‡</sup>NanoView Biosciences, Boston, Massachusetts 02215, United States

## S Supporting Information

**ABSTRACT:** DNA and protein microarrays are a high-throughput technology that allow the simultaneous quantification of tens of thousands of different biomolecular species. The mediocre sensitivity and limited dynamic range of traditional fluorescence microarrays compared to other detection techniques have been the technology's Achilles' heel and prevented their adoption for many biomedical and clinical diagnostic applications. Previous work to enhance the sensitivity of microarray readout to the single-molecule ("digital") regime have either required signal amplifying chemistry or sacrificed throughput, nixing the platform's primary advantages. Here, we report the development of a digital microarray which extends both the sensitivity and dynamic range of microarrays by about 3 orders of magnitude. This technique uses functionalized gold nanorods as single-molecule labels and an interferometric scanner which can rapidly enumerate individual nanorods by imaging them with a 10× objective lens. This approach does not require any chemical signal enhancement such as silver deposition and scans arrays with a throughput similar to commercial fluorescence scanners. By combining single-nanoparticle enumeration and ensemble measurements of spots when the particles are very dense, this system achieves a dynamic range of about 6 orders of magnitude directly from a single scan. As a proof-of-concept digital protein microarray assay, we demonstrated detection of hepatitis B virus surface antigen in buffer with a limit of detection of 3.2 pg/mL. More broadly, the technique's simplicity and high-throughput nature make digital microarrays a flexible platform technology with a wide range of potential applications in biomedical research and clinical diagnostics.

**KEYWORDS:** biosensing, DNA chip, multiplexed immunoassay, high-throughput imaging, nanoparticles



Protein and DNA microarray technologies continue to be useful in a myriad of biomedical and clinical applications, such as high-throughput genetic or transcriptional analysis and multiplexed protein detection. Insufficient sensitivity and dynamic range are the two most commonly cited weaknesses of the technology and have motivated the widespread adoption of newer methods based on DNA sequencing or sample compartmentalization to perform sensitive and multiplexed nucleic acid or protein analysis.<sup>1–3</sup>

The oft-cited explanation for their low sensitivity is that microarrays are a type of "solid-phase" biosensor, in which analyte molecules must diffuse across micron- to millimeter-scale distances to reach the planar chip in order to be detected. The time required for such sensors to reach equilibrium with a low-concentration analyte is dominated by the rate of mass transport, even in the presence of mixing. The result is that microarray experiments require long incubation times, and even

overnight incubations are not long enough to detect the lowest-abundance species.

In practice, however, this mass transport limitation is drastically worsened by the low readout sensitivity of commercial microarray scanning instrumentation. Once captured by the sensor, the analyte molecules must be quantified by fluorescence labeling or other means. Most commercial instruments require thousands of fluorophores per microarray spot to register a positive signal and have a usable dynamic range of around 100–1,000.<sup>4–6</sup> This is compared to a theoretically ideal transducer which reported the exact number of captured analyte molecules. Since a typical 100  $\mu\text{m}$ -wide microarray spot can contain up to 1 billion binding sites,<sup>7</sup> this theoretical transducer would have a readout sensitivity limited

**Received:** March 18, 2018

**Accepted:** May 14, 2018

**Published:** May 14, 2018

only by Poisson variability and a readout dynamic range as high as 100 million.

This enormous discrepancy between theoretical and practical performance in microarray readout technology stems from the physical and optical requirements for single-fluorophore detection. Enumerating single molecules with fluorescence labeling is now a routine process and has been used extensively to develop ultrasensitive biosensors for a wide variety of applications, for example, single-molecule pull-down (SIMPull) co-immunoprecipitation for studying protein–protein interactions,<sup>8</sup> Förster resonance energy-transfer measurements of individual molecular interactions,<sup>9,10</sup> single-molecule counting protein microarrays for protein expression analysis,<sup>11–13</sup> and single-molecule DNA microarrays for quantification of low-abundance RNA and DNA.<sup>14,15</sup> These techniques do indeed close the performance gap described earlier. Combining single-molecule counting with total fluorescence measurements has been shown to provide a usable dynamic range as high as 1 million and a detection limit near or below 1 femtomolar.<sup>16,17</sup>

However, these gains come at the expense of multiplexing and throughput. Regardless of the excitation modality, all of these techniques require a high numerical aperture ( $NA \geq 0.8$ ) objective lens to collect enough light to detect the individual fluorescence signals. Provided that the transverse lens size is fixed, one cannot increase light collection efficiency without decreasing the objective focal length. This reduces the field of view of the instrument to a small area (typically  $0.01\text{--}0.1\text{ mm}^2$ ) and necessitates precise focusing (typically within  $300\text{ nm}$ ). In contrast, a typical commercial DNA microarray has a matrix of around 100,000 spots across a  $1\text{ cm}^2$  area and must be scanned in a matter of minutes by a cost-effective instrument.

It is technically possible to scan a full-sized fluorescence microarray with single-fluorophore sensitivity. Schültz and colleagues have achieved this by combining a  $100\times$  oil-immersion objective, time delay and integration-mode CCD and precision XY positioners for continuous-motion acquisition, and a closed loop two-stage piezo and motorized focus locking system.<sup>18,19</sup> Even then, however, the performance envelope remains fundamentally limited by the quantum “speed limit” of the fluorophore’s emission lifetime, which sets the fluorophore’s minimum obtainable emission rate and therefore minimum required observation time. It remains to be seen whether a single-fluorophore, whole-slide scanner can be deployed with a price and throughput competitive with existing benchtop scanners, which simply use low-NA objectives to achieve the necessary speed and robustness.

In contrast, measurements of light scattering by nanoparticles have no saturated emission rate or photobleaching. The speed and throughput of light scattering measurements should in principle be limited only by the available light power or maximum allowable local heating of the particle due to absorption. This has motivated the use of gold nanoparticle-functionalized probes in place of fluorescent probes for microarray labeling, which are either detected individually directly based on their light scattering<sup>20–28</sup> or indirectly *via* silver deposition.<sup>29–32</sup> Similar to the fluorescence-based techniques mentioned earlier, these nanoparticle-based techniques have also successfully enhanced the dynamic range of microarrays by several orders of magnitude and typically have a limit of detection of roughly 1 femtomolar. However, direct detection of nanoparticle labels has only been done with a high-NA lens, resulting in the same throughput limitations as single-molecule fluorescence. Silver enhancement and colorimetric

detection, on the other hand, enables both high sensitivity and high throughput, but multiple rounds of silver enhancement and rescanning are required to achieve a higher dynamic range.<sup>33</sup>

To our knowledge, no method exists to enumerate individual nanoparticle labels across a very large surface with a throughput comparable to commercial microarray scanners. The most obvious way to increase throughput would be to use a lower magnification lens to increase the instrument field of view. However, lower magnification lenses have a lower NA and are less efficient at collecting light, and reduced light collection is unacceptable for many single-fluorophore detection schemes. For dark-field detection, the signal scales (approximately, for  $NA < 0.6$ ) with the fourth power of the NA. Similarly, the rejection of out-of-focus background light in confocal systems is greatly reduced by reducing NA, as the confocal depth increases with square of the NA.

Interferometric detection is more resilient than dark-field to very weak signals since the scattered light amplitude is measured rather than intensity. Interferometric reflectance imaging sensing (IRIS) is one of a family of similar optical techniques for interferometric detection of nanoparticles immobilized on a substrate.<sup>24,34,35</sup> IRIS uses a substrate of polished silicon with a transparent thin film, typically thermally grown silicon dioxide. The substrate is imaged with a reflectance microscope with Köhler illumination from an LED source. In the absence of any nanoparticle, the microscope camera observes a featureless reflection of the illumination light on the substrate surface. If a nanoparticle is present, light scattered by the particle is also imaged onto the camera where it forms a faint diffraction-limited interference pattern with the reflected light. The “normalized intensity” of this interference pattern is obtained by dividing by the intensity of the reflected field alone.

If the substrate and illumination were both ideally smooth and uniform, arbitrarily weak signals could be detected by collecting enough photons until the shot noise was reduced below the normalized intensity of the signal. In practice, IRIS substrates are slightly heterogeneous, resulting in about 0.5% fluctuations in reflectivity across the chip surface. Therefore, the normalized intensity of nanoparticles must be at least about 1–2% to be robustly detected.

This is the main challenge to performing interferometric detection with a low-NA objective—reducing the NA reduces the collection of scattered light but not that of reflected light, which reduces the normalized intensity of the particle image. If the normalized intensity drops below the visibility threshold (about 1%), the particle will no longer be detectable with IRIS. The reduced scattering could be compensated for if the reflected light could be attenuated. However, this cannot be done with a simple neutral density filter since it takes the same optical path from the chip surface to the camera and requires pupil function modification.<sup>36</sup> If the target nanoparticles are naturally occurring such as viruses and exosomes, we cannot control their light scattering properties, and thus visibility enhancement methods are limited to modifications in the optical system. When artificial nanoparticles are used as labels, the visibility enhancement can utilize tailoring scattering properties of the nanoparticles, along with the optical imaging platform. In this work we developed a method that utilizes the depolarization properties of plasmonic gold nanorods and polarization microscopy techniques to selectively attenuate the reflected light. As a result, we demonstrate nanoparticle

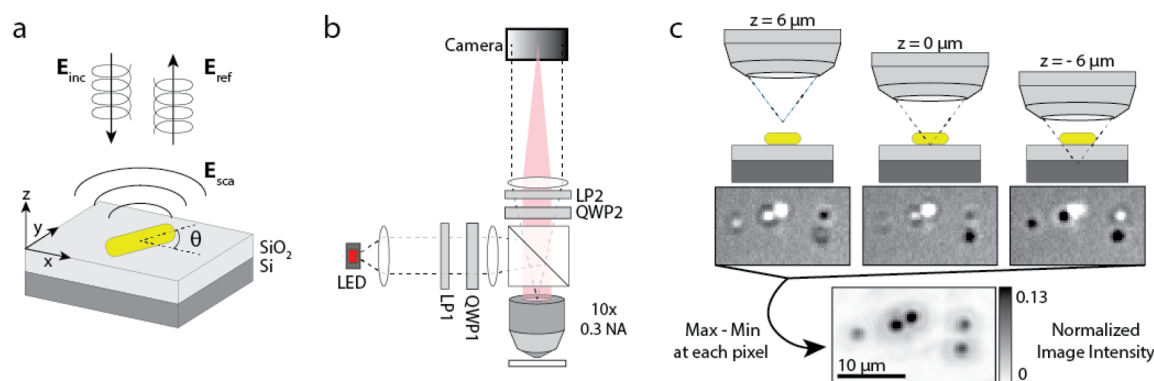


**Figure 1.** (a) Schematic of GNR detection with IRIS. Circularly polarized plane wave illumination  $E_{inc}$  is reflected as a circularly polarized plane wave by the IRIS substrate  $E_{ref}$  but scattered by the GNR as a spherical wave  $E_{sca}$  that is linearly polarized along the rod's longitudinal axis  $\theta$ . (b) Schematic of the reflectance microscope used to image the IRIS chip. Both the reflected (dotted lines) and scattered light (red shadow) are imaged onto the camera with a 10 $\times$  objective (LP, linear polarizer; QWP, quarter wave plate). (c) At the camera, the phase between scattered and reflected light depends on both particle orientation  $\theta$  and focus position  $z$ . All GNRs are robustly detected regardless of their orientation by acquiring a  $z$ -stack and measuring the difference between the maximum and minimum normalized intensity observed at each  $(x,y)$  pixel.

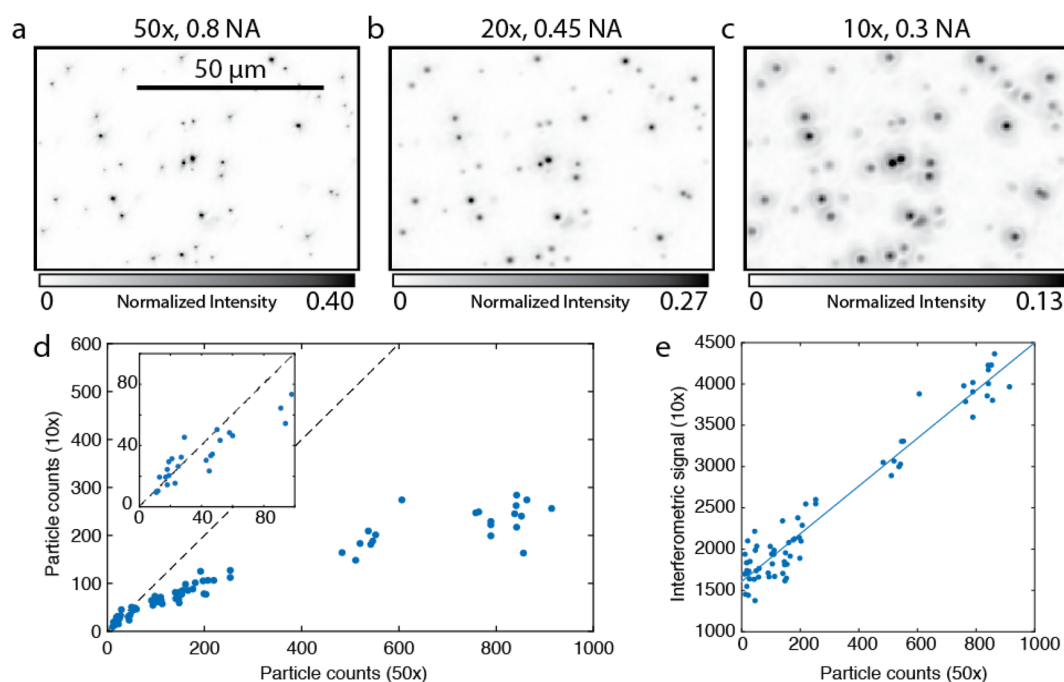


**Figure 2.** Validation of GNR quantification. GNRs on an IRIS substrate imaged with (a) 50 $\times$ , (b) 20 $\times$ , and (c) 10 $\times$  objective lenses. Individual nanorods are visible as diffraction-limited spots, which are the size and shape of the system's point spread function. Provided they are not too close to one another, all nanorods visible in (a) are also visible in (b) and (c). (d) Scatter plot of the number of particles counted within 70 different spots (cropped to  $1e4 \mu m^2$ ), with 10 $\times$  vs 50 $\times$  objective lenses. While the two magnifications are in good agreement when the number of GNRs is low (inset), the lower resolution of the 10 $\times$  objective results in systematic under-counting when there are over 60 particles per spot. (e) Scatter plot of total interferometric signal (*i.e.*, sum of normalized intensity at all pixels within each spot) of the same 70 spots vs number of particles counted with a 50 $\times$  lens. The interferometric signal is proportional to GNR number when there are over 200 particles.

detection with good visibility across a very wide field of view with a modest numerical aperture objective (10 $\times$ , 0.3 NA).

## RESULTS AND DISCUSSION

**Interferometric Detection of Single Plasmonic Nanorods with a 10 $\times$ , 0.3 NA Objective Lens.** Plasmonic GNRs are rod-shaped nanoparticles with the interesting optical property that their scattering cross section is a function of both wavelength and polarization. At its longitudinal surface plasmon resonance wavelength, a GNR effectively only scatters

the component of the excitation that is polarized along its longitudinal axis.<sup>37</sup>

Consider a nanorod on an IRIS substrate illuminated by circularly polarized plane wave at normal incidence ( $E_{inc}$ , Figure 1a). Light reflected by the substrate ( $E_{ref}$ ) remains circularly polarized, but the light scattered by the particle ( $E_{sca}$ ) will be linearly polarized. This discrepancy between the polarizations of the scattered and reflected light can be exploited to selectively attenuate the reflected light with a quarter wave plate and linear polarizer in the imaging path (QWP2 and LP2,

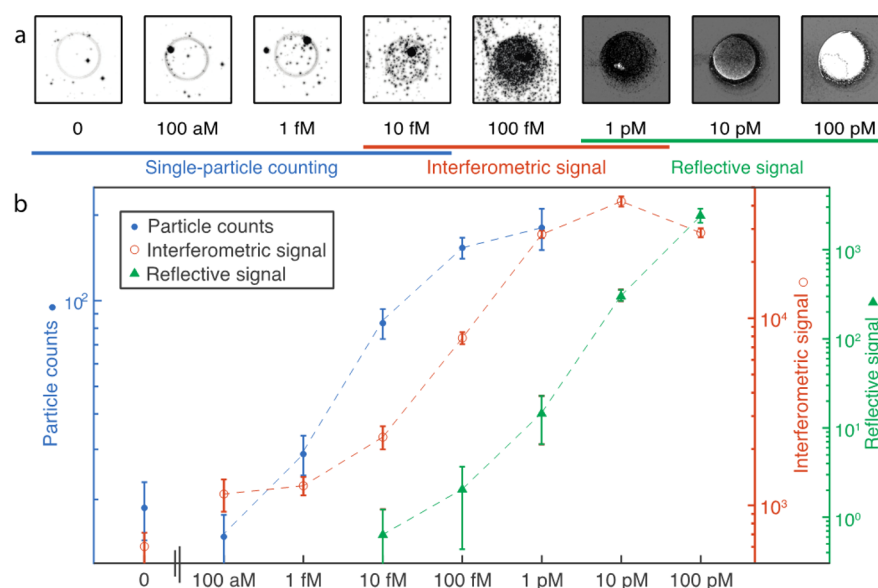


**Figure 3.** (a) DNA microarray spots on eight different IRIS substrates after incubation for 4 h with GNRs conjugated with the complementary sequence at a range of concentrations. (b) Log–log standard curves of the number of individual particles counted, average interferometric signal, and reflective signal per spot (described in text). Error bars indicate one standard deviation ( $n = 10$  spots per chip).

Figure 1b). These two optics are adjusted to attenuate the reflected light amplitude by precisely 95%, while attenuating the scattered light amplitude by only 30–50%, depending on polarization direction. This has the effect of increasing the normalized intensity of the GNRs by about 7–10-fold, depending on the particle's surface orientation angle  $\theta$  (Figure S1). These optics also retard the phase of the scattered light by different amounts, depending on  $\theta$ . This variable phase shift causes particles of different orientations to appear darker than the background, or brighter, or nearly invisible when the two fields are in quadrature (Figure 1c). Fortunately, changing the focus position also changes the path length difference between the scattered and reflected light. All particles are made visible by taking a  $z$ -stack of images and then subtracting the minimum value from the maximum value at each  $(x,y)$  pixel location (Figure 1c). This mechanism is described in detail elsewhere,<sup>35</sup> but it essentially requires that the illumination is aligned so as to radically under-fill the back pupil of the objective and approximate a plane wave at the chip surface.

**Co-Optimization of the Optical System for Rapid GNR Detection.** The oxide film thickness of the substrate, illumination wavelength, and nanorod geometry all effect the amplitude of the scattered light collected by the objective. We used a quantitative model of interferometric reflectance imaging described previously to co-optimize these various parameters and guide the selection of 25 nm diameter GNRs with a longitudinal surface plasmon resonance wavelength of 650 nm, a substrate oxide thickness of 110 nm, and 650 nm LED illumination source with an 10 nm fwhm bandpass filter (Figure S2).<sup>35</sup> Early on in this study, we also compared the circular polarization scheme described here with a simpler cross-polarization scheme, in which the illumination is linearly polarized rather than circularly polarized and mostly blocked by a crossed polarizer in the collection path (Figure S3). However, we found that only particles with certain surface orientations were made more visible using the cross-polarization scheme, while the circular polarization scheme enhanced the visibility of rods of all orientations.

Once the optical design was finalized, we experimentally determined the optimal amount of attenuation for the rapid detection of GNRs. We initially observed that the noise floor of the image began to increase noticeably when the analyzer (LP2, Figure 1b) was adjusted to attenuate over 99% of the reflected light. Attenuating the reference increases the normalized intensity of the particle, but also lowers the intensity of the collected light, which necessitates a longer exposure time to collect the same number of photons. In our apparatus, back reflections from the cube beam splitter were the main source of stray light and had a relative intensity of about 1% of the illumination (Figure S4). We found that setting the analyzer to extinguish precisely 95% of the reflected light was enough to enhance the normalized intensity the GNRs until they were clearly distinguishable against the background, without substantially increasing the noise floor.

**Validation of Single GNR Counting with a 10 $\times$ , 0.3 NA Objective.** To experimentally measure the visibility of GNRs with large field-of-view objectives, 25 nm  $\times$  71 nm rods were sparsely immobilized onto an IRIS substrate, which was dried and imaged with 10 $\times$ , 20 $\times$ , and 50 $\times$  objective lenses (Figure 2a–c). All individual nanorods that were visible in the 50 $\times$  frame were also easily visible in those frames taken by the 20 $\times$  and 10 $\times$  objective lenses, provided the particles were far enough apart from one another to be distinguished.

We anticipated that the low-magnification system would be able to accurately count nanoparticles when they were very sparse but would under-count them as the nanoparticle surface density increased, because particles closer than the Abbe limit (about 1.1  $\mu$ m for the 10 $\times$ , 0.3 NA objective) would be indistinguishable. To investigate this, we printed microarrays of poly adenine (14-A) single-stranded DNA oligonucleotides on IRIS substrates and conjugated gold nanorods with poly thymine (14-T) single-stranded DNA. The conjugated GNRs were diluted to a range of concentrations between 100 attomolar and 100 picomolar, then incubated with the DNA chips for 4 h, and then finally washed and dried. A total of 70 spots were imaged with instrument using both the 10 $\times$  and 50 $\times$  objectives, and images were analyzed using custom particle



analysis software described previously.<sup>38</sup> As expected, the 10× objective system accurately enumerated immobilized GNRs when they were few (*i.e.*, 60 GNR per spot or fewer), but systematically under-counted as their number increased (Figure 2d). This was recapitulated by a simple model of particle crowding, in which GNRs in the image are modeled as disks placed randomly in an image with uniform probability, and any overlapping disks are “detected” as a single particle. In the model, accuracy was improved by measuring and compensating for the average rate of under-counting due to particle crowding (Figure S5). Although this is a statistical method, such an approach may be useful at improving the absolute accuracy in the range of 50–200 particles, where undercounting is significant yet somewhat predictable.

**GNR Quantification at High Densities.** Above 200 GNR per spot, accurate enumeration of GNRs becomes impossible due to severe crowding. However, the number of GNRs within an image region are accurately estimated by simply summing the total normalized intensity of all pixels in that region. We call this the “interferometric signal” since it is a measurement of the total *amplitude* (rather than intensity) of scattered light. To validate that the interferometric signal scales linearly with the number of nanoparticles, we compared the interferometric signal with the number of GNRs, as detected with a 50× objective, in the 70 microarray spots described earlier (Figure 2e). We found that the interferometric signal is proportional to GNR number when there are at least 200 GNRs per spot. This background is a consequence of other non-GNR light scattering nanostructures on the chip surface such as the boundary of the microarray DNA spot itself (visible in Figure 3a and Figure 4). These nanostructures are easily filtered based on their size and shape when performing single-GNR counting, but not when measuring the total interferometric signal.

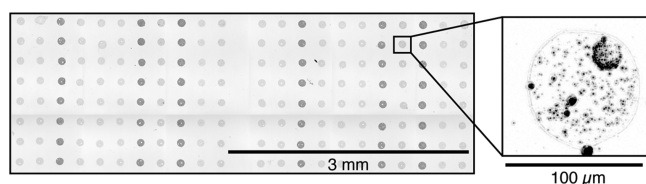


**Figure 4.** A composite image of an IRIS microarray scanned by the automated digital microarray instrument. The instrument has a scan speed of about 3 mm<sup>2</sup> (50–125 spots) per minute, similar to most commercial fluorescence scanners.

On the highest concentration chips (10–100 pM), GNRs were packed sufficiently close together to lose their plasmonic scattering properties and acted like a highly reflective gold film (Figure 3a). In those cases, the total interferometric light scattering signal actually decreases, despite the spots becoming visible to the naked eye. We found we were able to robustly quantify the reflectivity of a spot simply by taking the average value of the *z*-stack at each (*x,y*) position (rather than the maximal difference for interferometric detection, as in Figure 1c) and then normalizing by and subtracting the reflectivity of the bare chip.

These three quantification methods, single GNR counting, total interferometric signal, and total reflective signal, are complementary since they each quantify GNR binding within different ranges of concentration (Figure 3b). By combining them, the instrument achieves both single-nanoparticle readout

sensitivity and a dynamic range of nearly one million from a single scan.

Importantly, all three of these measurements are obtained from the same image data. Most other methods to achieve a large dynamic range require rescanning the array multiple times, either after multiple rounds of silver enhancement,<sup>33</sup> changing the objective lens, or changing the exposure time in the case of fluorescence.<sup>16</sup>

We next incorporated a motorized stage and automation software into the instrument to demonstrate the utility of this technique for larger arrays. The 10× objective provides a field of view of 1.46 mm<sup>2</sup>, large enough to fit between 24 and 63 spots with a spot pitch of 250 or 150 μm, respectively. To scan larger arrays, the region of interest is divided into tiles that are sequentially scanned and then combined (Figure 4). Image acquisition takes about 30 s per field of view and is primarily limited in speed by the amount of available light power from the 940 mW LED source. A brighter illumination source could enable the same acquisition in about 5 s. With current settings, the instrument would be able to scan a 1 cm<sup>2</sup> array in about 35 min, or a very large array with 15,000 spots and a 150 μm pitch in about 2 h (a brighter source could lower this to 5 and 20 min, respectively).

The acquired image data are then processed using custom-built analysis software. The application performs semi-automated spot finding and segmentation and provides measurements of the number of GNRs, interferometric signal, and reflective signal within each spot. These three numbers are combined into a single measurement through a simple sequential algorithm: If the reflective signal is above the background threshold, then use the reflective signal lookup table; otherwise, if the interferometric signal is above the background threshold, then use the interferometric signal lookup table; otherwise, use the single-particle counting signal. These background thresholds must be calibrated using standard samples of known concentrations.

#### Sensitive Protein Detection with Digital Microarrays.

In addition to DNA microarrays, digital microarray readout may also improve the sensitivity and dynamic range of multiplexed protein detection with antibody microarrays. To demonstrate this, we developed a proof-of-concept digital microarray assay for hepatitis B virus surface antigen (HBsAg, Figure 5). Hepatitis B viral infection has worldwide significance with annual mortalities in excess of 300,000, and HBsAg is a reliable biomarker of viral hepatitis both for early detection of infection and for monitoring response to antiretroviral therapy.<sup>39</sup>

Briefly, protein microarrays of HBsAg antibody spots and bovine serum albumin (BSA) control spots were prepared on IRIS chips as described in the [Methods](#) section. Chips were incubated for 2.5 h with the antigen, followed by 2 h of incubation with antibody-functionalized GNRs. Finally, the chips were dried and imaged with the automated scanner instrument to count the number of GNRs on both HBsAg antibody and BSA control spots. These experiments did not have a blank sample negative control, so we estimated the assay's lower limit of detection based on the number of GNRs nonspecifically binding to BSA spots to be about 3.2 pg/mL. The assay's coefficient of variation was about 13%.

## CONCLUSIONS

Digital microarrays greatly improve upon the sensitivity and dynamic range of conventional fluorescence microarrays, while

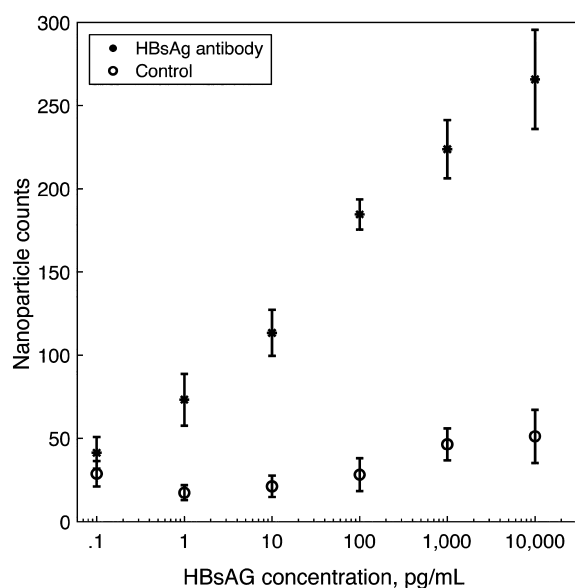


**Figure 5. Digital microarrays for sensitive protein quantification.** An assay for hepatitis B virus surface antigen ( $n = 6$  spots per condition per chip).

maintaining their advantages in high multiplexing and low cost. Our approach combines gold nanoparticle labels with an interferometric detector to achieve single-molecule reporting capability without sacrificing high-throughput acquisition of typical centimeter-scale microarrays.

IRIS digital microarrays may be used to quantify both nucleic acids and proteins with high sensitivity. We anticipate this technique will have utility in applications that require both high sensitivity and high multiplexing capability, such as in detecting rare cell-free DNA mutations for cancer diagnostics.<sup>40</sup> Since the sensitivity of digital microarrays may be increased by adding duplicate spots for each probe condition to increase the sensor surface area, this high-throughput method may also have utility even when the number of probes is few, but very high sensitivity is required. The instrument and processes are no more complex or costly than commercial fluorescence microarrays, so it may be deployed in similar research or clinical diagnostic settings. In terms of assay compatibility and performance, this technique is fully compatible with the protocols in literature that use gold nanoparticle labels to detect RNA,<sup>33</sup> DNA,<sup>29</sup> and proteins.<sup>22</sup> For nucleic acid analysis, we expect it would have the similar sensitivity and limits of detection (in the range of 100 attomolar to 1 femtomolar) since the biochemical aspects are identical to these previously published works. The ability to scan large areas can in principle also be leveraged to increase sensitivity further by scanning many replicate spots.

Altogether, digital microarrays are a platform technology with a range of potential applications. We are currently focused on further evaluating and developing the proof-of-concept HBsAg assay with complex sample matrices as well as investigating further applications of the digital microarray technique in gene expression analysis.

## METHODS

**IRIS Microarray Substrate Preparation.** IRIS chips were fabricated by performing 110 nm of thermal oxide growth, photolithographic patterning, and oxide etching on polished silicon wafers (Silicon Valley Microelectronics, Santa Clara CA). Chips were

coated with a copolymer designed for high density immobilization of 5' amine-modified DNAs onto glass substrates (MCP-4, Lucidant Polymers, Sunnyvale CA). For DNA microarray preparation, amine-terminated DNA probes were purchased from Integrated DNA Technologies (Coralville, IA) and printed onto the chips with a SCIENION, Inc. S3 FlexArrayer in 150 mM sodium phosphate buffer, pH 8.5. For protein microarray preparation, monoclonal HBsAg antibody (10-H05H Fitzgerald, Acton, MA) and bovine serum albumin were both spotted at concentrations of 3 mg/mL in phosphate buffered saline pH 7.4 (PBS) containing 25 mM trehalose. Individual droplet sizes of 200–250 pL and a spotting chamber humidity of 67% were found to yield the roundest and most even spots for both antibody and DNA immobilization. Chips were left in the spotter humid chamber overnight and washed the next morning. Both DNA and protein microarray chips were washed three times in large volumes of 1× PBS for 5 min each time. DNA microarrays were also subsequently washed once in DI water. Chips were dried by blowing the array with compressed nitrogen and stored in a desiccator at room temperature for up to one month.

**Gold Nanorod Functionalization with DNA and Microarray Hybridization.** For DNA functionalization, citrate-stabilized 25 nm by 71 nm GNRs were purchased from Nanopartz, Inc. (Loveland, CO) and conjugated with the universal label sequences using the “fast acid” protocol published by others.<sup>41</sup> Briefly, GNRs were washed twice in DI water to remove excess citrate by centrifugation at 1500 rcf for 15 min. 14-A DNA oligonucleotides with thiol-modified 5' ends from Integrated DNA Technologies were deprotected using dithiothreitol as per manufacturer instructions and combined with GNRs in DI water at a DNA concentration of 500 nM and GNR concentration of approximately 500 pM. The solution was stored in a glass vial wrapped in foil on an orbital shaker at room temperature for 15 min. The pH was then adjusted to 3.0 with 10 mM sodium citrate buffer, again rested for 15 min on the shaker, and then Tween-20 was added to a final concentration of 0.1% w/v. The sodium chloride concentration of the solution was gradually increased to 150 mM over the course of 4 h through four additions of concentrated sodium chloride. The GNR solution was vortexed and sonicated very briefly before and after each salt addition. The solution was left on the shaker plate overnight and then washed five times in 1× PBST (1× phosphate buffered saline with 0.1% Tween-20) by centrifugation to remove excess unbound DNA.

For hybridization, GNRs were diluted to final concentrations in PBST with 600 mM total NaCl, 0.1% Tween-20, and 1 mM EDTA. IRIS microarray chips (1 cm<sup>2</sup> size) were placed individually into 24-well plate with 250  $\mu$ L of GNR solution and placed on the orbital shaker at room temperature for 4 h. Chips were washed once in separate small Petri dishes of the hybridization buffer, followed by twice in PBS with 600 mM NaCl (but without Tween), then finally twice with PBS. Washes were performed for 90 s each, and chips were transferred between Petri dishes taking care not to let the chip surface dry and withdrawn from the final wash at a steep angle to minimize liquid retention on the array. Chips were blown with nitrogen to dry completely and imaged using the automated IRIS instrument as described below.

**Gold Nanorod Functionalization with Antibodies and HBsAg Detection.** For antibody functionalization, 15 nm by 40 nm carboxyl-modified gold nanorods were purchased from CytoDiagnostics, Inc. (Burlington, CA) and conjugated with polyclonal HBsAg antibody (70-HG15S Fitzgerald) following the manufacturer's kit instructions. For HBsAg detection, the IRIS protein microarray chips were first incubated for 2.5 h with HBsAg ad protein (30AH15 Fitzgerald) diluted in stain buffer (FBS), which contains 2% fetal bovine serum and <0.09% sodium azide (BD Biosciences, San Jose, CA). As before, incubations were performed in 24-well plates with 250  $\mu$ L of sample solution per well. Chips were washed just once with PBS for 90 s and dried using the same protocol described above. Chips were then incubated at room temperature on the orbital shaker with the antibody-functionalized GNRs in PBS for 2 h at a concentration of about 10 picomolar, again in a 24-well plate. Finally, chips were washed twice in PBS, dried, and imaged as described below.

**Image Acquisition and analysis.** The automated instrument was controlled using custom scripts and plugins for Micromanager, an open-source microscope control application.<sup>42</sup> With the 10× objective, a z-stack of 15 frames with a 3 μm step size was acquired. With the 50× objective, 16 frames were acquired with a 250 nm step size. At each z position, 16 frames were acquired and immediately averaged before saving to reduce shot noise.

The reflectance image described in text was acquired from the z-stack images by simply taking the average grayscale value of each (x,y) pixel through the stack. The interferometric image, on the other hand, requires additional filtering to reduce noise. Each frame of the z-stack is smoothed using a sparse pseudomedian filter with a kernel selected to be slightly larger than the image point spread function. All images are normalized by the median value of all images. Then, the difference between the maximum and minimum grayscale values at each (x,y) pixel position is determined. This is the “interferometric image” as described in the text.

Nanoparticles in the image are detected by (1) performing a cross-correlation with a measured image kernel, (2) binarization of the image with a predetermined global threshold, and (3) filtering of keypoints based on size and area-to-perimeter ratio to include only diffraction limited blobs. Keypoint filtering thresholds were iteratively optimized by hand once and then applied identically to all images.

All image acquisition and processing software described here has been made freely available online at <https://github.com/derinsevenler/spandex>.

## ASSOCIATED CONTENT

### Supporting Information

The Supporting Information is available free of charge on the ACS Publications website at DOI: 10.1021/acsnano.8b02036.

Figure S1, numerical simulation results of gold nanorod imaging with the digital microarray instrument; Figure S2, simulation-based optimization of the IRIS substrate to maximize nanorod visibility; Figure S3, schematic of the similar but inferior design based on cross-polarization; Figure S4, experimental optimization of attenuation amount; Figure S5, a computational model of particle crowding in IRIS images (PDF)

## AUTHOR INFORMATION

### Corresponding Author

\*E-mail: [derin@bu.edu](mailto:derin@bu.edu).

### ORCID

Derin Sevenler: 0000-0002-0327-5638

### Notes

The authors declare no competing financial interest.

## ACKNOWLEDGMENTS

The authors wish to thank Oguzhan Avci and Jacob Trueb for thoughtful comments and suggestions regarding numerical optimization of the optical system. This work was funded in part by a research contract with ASELSAN, Inc. and the Wallace H. Coulter Foundation 2010 Coulter Translational Award.

## REFERENCES

(1) Mestdagh, P.; Hartmann, N.; Baeriswyl, L.; Andreasen, D.; Bernard, N.; Chen, C.; Cheo, D.; D'Andrade, P.; DeMayo, M.; Dennis, L.; Derveaux, S.; Feng, Y.; Fulmer-Smentek, S.; Gerstmayer, B.; Gouffon, J.; Grimley, C.; Lader, E.; Lee, K. Y.; Luo, S.; Mouritzen, P.; et al. Evaluation of Quantitative MiRNA Expression Platforms in the MicroRNA Quality Control (MiRQC) Study. *Nat. Methods* **2014**, *11*, 809–815.

(2) Wang, Z.; Gerstein, M.; Snyder, M. RNA-Seq: A Revolutionary Tool for Transcriptomics. *Nat. Rev. Genet.* **2009**, *10*, 57–63.

(3) Baker, M. Digital PCR Hits Its Stride. *Nat. Methods* **2012**, *9*, 541–544.

(4) Shi, L.; Tong, W.; Su, Z.; Han, T.; Han, J.; Puri, R. K.; Fang, H.; Frueh, F. W.; Goodsaid, F. M.; Guo, L.; Branham, W.; Chen, J.; Xu, Z. A.; Harris, S. C.; Hong, H.; Xie, Q.; Perkins, R. G.; Fuscoe, J. C. Microarray Scanner Calibration Curves: Characteristics and Implications. *BMC Bioinf.* **2005**, *6*, S11.

(5) Pozhitkov, A. E. Scanner Calibration Revisited. *BMC Bioinf.* **2010**, *11*, 361.

(6) Risinger, A.; Williams, C. *ScanArray GX PLUS/ProScanArray Competitive Performance Analysis Using a Commercial Test Slide*; Application Note; Perkin Elmer: Boston, MA, 2006.

(7) Ozkumur, E.; Yalcin, A.; Cretich, M.; Lopez, C. A.; Bergstein, D. A.; Goldberg, B. B.; Chiari, M.; Ünlü, M. S. Quantification of DNA and Protein Adsorption by Optical Phase Shift. *Biosens. Bioelectron.* **2009**, *25*, 167–172.

(8) Aggarwal, V.; Ha, T. Single-molecule Pull-down (SiMPull) for New-age Biochemistry. *BioEssays* **2014**, *36*, 1109–1119.

(9) Lamichhane, R.; Solem, A.; Black, W.; Rueda, D. Single-Molecule FRET of Protein–nucleic Acid and Protein–protein Complexes: Surface Passivation and Immobilization. *Methods* **2010**, *52*, 192–200.

(10) Roy, R.; Hohng, S.; Ha, T. A Practical Guide to Single-Molecule FRET. *Nat. Methods* **2008**, *5*, 507–516.

(11) Li, L.; Qu, X.; Sun, J.; Yang, M.; Song, B.; Shao, Q.; Zhang, X.; Jin, W. Single-Molecule-Counting Protein Microarray Assay with Nanoliter Samples and Its Application in the Dynamic Protein Expression of Living Cells. *Biosens. Bioelectron.* **2011**, *26*, 3688–3691.

(12) Tessler, L. A.; Reifenger, J. G.; Mitra, R. D. Protein Quantification in Complex Mixtures by Solid Phase Single-Molecule Counting. *Anal. Chem.* **2009**, *81*, 7141–7148.

(13) Tessler, L. A.; Mitra, R. D. Sensitive Single-Molecule Protein Quantification and Protein Complex Detection in a Microarray Format. *Proteomics* **2011**, *11*, 4731–4735.

(14) Hesse, J.; Jacak, J.; Kasper, M.; Regl, G.; Eichberger, T.; Winklmayr, M.; Aberger, F.; Sonnleitner, M.; Schlapak, R.; Howorka, S.; Muresan, L.; Frischauf, A.; Schütz, G. J. RNA Expression Profiling at the Single Molecule Level. *Genome Res.* **2006**, *16*, 1041–1045.

(15) Haider, M.; Ji, B.; Haselgrübler, T.; Sonnleitner, A.; Aberger, F.; Hesse, J. A Microfluidic Multiwell Chip for Enzyme-Free Detection of mRNA from Few Cells. *Biosens. Bioelectron.* **2016**, *86*, 20–26.

(16) Rissin, D. M.; Fournier, D. R.; Piech, T.; Kan, C. W.; Campbell, T. G.; Song, L.; Chang, L.; Rivnak, A. J.; Patel, P. P.; Provuncher, G. K.; Ferrell, E. P.; Howes, S. C.; Pink, B. A.; Minnehan, K. A.; Wilson, D. H.; Duffy, D. C. Simultaneous Detection of Single Molecules and Singulated Ensembles of Molecules Enables Immunoassays with Broad Dynamic Range. *Anal. Chem.* **2011**, *83*, 2279–2285.

(17) Sonnleitner, M.; Freudenthaler, G.; Hesse, J.; Schütz, G. J. High-Throughput Scanning with Single-Molecule Sensitivity. *Proc. SPIE* **2005**, *5699*, 202–210.

(18) Hesse, J.; Sonnleitner, M.; Sonnleitner, A.; Freudenthaler, G.; Jacak, J.; Höglinger, O.; Schindler, H.; Schütz, G. J. Single-Molecule Reader for High-Throughput Bioanalysis. *Anal. Chem.* **2004**, *76*, 5960–5964.

(19) Hesch, C.; Hesse, J.; Jacak, J.; Schütz, G. J. Two-Stage Focus-Hold System for Rapid Ultra-Sensitive Read-out of Large-Area Biochips. *J. Microsc.* **2009**, *234*, 251–254.

(20) Morozov, V. N.; Groves, S.; Turell, M. J.; Bailey, C. Three Minutes-Long Electrophoretically Assisted Zeptomolar Microfluidic Immunoassay with Magnetic-Beads Detection. *J. Am. Chem. Soc.* **2007**, *129*, 12628–12629.

(21) Blab, G. A.; Cognet, L.; Berciaud, S.; Alexandre, I.; Husar, D.; Remacle, J.; Lounis, B. Optical Readout of Gold Nanoparticle-Based DNA Microarrays without Silver Enhancement. *Biophys. J.* **2006**, *90*, L13–L15.

(22) Monroe, M. R.; Daaboul, G. G.; Tuysuzoglu, A.; Lopez, C. A.; Little, F. F.; Ünlü, M. S. Single Nanoparticle Detection for Multiplexed



Protein Diagnostics with Attomolar Sensitivity in Serum and Unprocessed Whole Blood. *Anal. Chem.* **2013**, *85*, 3698–3706.

(23) Lindfors, K.; Kalkbrenner, T.; Stoller, P.; Sandoghdar, V. Detection and Spectroscopy of Gold Nanoparticles Using Super-continuum White Light Confocal Microscopy. *Phys. Rev. Lett.* **2004**, *93*, 037401.

(24) Patskovsky, S.; Meunier, M. Reflected Light Microspectroscopy for Single-Nanoparticle Biosensing. *J. Biomed. Opt.* **2015**, *20*, 097001–097001.

(25) Halpern, A. R.; Wood, J. B.; Wang, Y.; Corn, R. M. Single-Nanoparticle Near-Infrared Surface Plasmon Resonance Microscopy for Real-Time Measurements of DNA Hybridization Adsorption. *ACS Nano* **2014**, *8*, 1022–1030.

(26) Li, G.; Zhu, L.; Wu, Z.; He, Y.; Tan, H.; Sun, S. Digital Concentration Readout of DNA by Absolute Quantification of Optically Countable Gold Nanorods. *Anal. Chem.* **2016**, *88*, 10994–11000.

(27) Sönnichsen, C.; Geier, S.; Hecker, N. E.; von Plessen, G.; Feldmann, J.; Dittlbacher, H.; Lamprecht, B.; Krenn, J. R.; Aussenegg, F. R.; Chan, V. Z.-H.; Spatz, J. P.; Möller, M. Spectroscopy of Single Metallic Nanoparticles Using Total Internal Reflection Microscopy. *Appl. Phys. Lett.* **2000**, *77*, 2949–2951.

(28) Nelson, B. P.; Grimsrud, T. E.; Liles, M. R.; Goodman, R. M.; Corn, R. M. Surface Plasmon Resonance Imaging Measurements of DNA and RNA Hybridization Adsorption onto DNA Microarrays. *Anal. Chem.* **2001**, *73*, 1–7.

(29) Hill, H. D.; Mirkin, C. A. The Bio-Barcode Assay for the Detection of Protein and Nucleic Acid Targets Using DTT-Induced Ligand Exchange. *Nat. Protoc.* **2006**, *1*, 324–336.

(30) Zhou, G.; Bergeron, S.; Juncker, D. High-Performance Low-Cost Antibody Microarrays Using Enzyme-Mediated Silver Amplification. *J. Proteome Res.* **2015**, *14*, 1872–1879.

(31) Liang, R.-Q.; Li, W.; Li, Y.; Tan, C.; Li, J.-X.; Jin, Y.-X.; Ruan, K.-C. An Oligonucleotide Microarray for MicroRNA Expression Analysis Based on Labeling RNA with Quantum Dot and Nanogold Probe. *Nucleic Acids Res.* **2005**, *33*, e17–e17.

(32) Taton, T. A.; Mirkin, C. A.; Letsinger, R. L. Scanometric DNA Array Detection with Nanoparticle Probes. *Science* **2000**, *289*, 1757–1760.

(33) Alhasan, A. H.; Kim, D. Y.; Daniel, W. L.; Watson, E.; Meeks, J. J.; Thaxton, C. S.; Mirkin, C. A. Scanometric MicroRNA Array Profiling of Prostate Cancer Markers Using Spherical Nucleic Acid–Gold Nanoparticle Conjugates. *Anal. Chem.* **2012**, *84*, 4153–4160.

(34) Jacobsen, V.; Stoller, P.; Brunner, C.; Vogel, V.; Sandoghdar, V. Interferometric Optical Detection and Tracking of Very Small Gold Nanoparticles at a Water-Glass Interface. *Opt. Express* **2006**, *14*, 405–414.

(35) Sevenler, D.; Avci, O.; Ünlü, M. S. Quantitative Interferometric Reflectance Imaging for the Detection and Measurement of Biological Nanoparticles. *Biomed. Opt. Express* **2017**, *8*, 2976–2989.

(36) Avci, O.; Adato, R.; Ozkumur, A. Y.; Ünlü, M. S. Physical Modeling of Interference Enhanced Imaging and Characterization of Single Nanoparticles. *Opt. Express* **2016**, *24*, 6094.

(37) Cao, J.; Sun, T.; Grattan, K. T. V. Gold Nanorod-Based Localized Surface Plasmon Resonance Biosensors: A Review. *Sens. Actuators, B* **2014**, *195*, 332–351.

(38) Trueb, J. T.; Avci, O.; Sevenler, D.; Connor, J. H.; Ünlü, M. S. Robust Visualization and Discrimination of Nanoparticles by Interferometric Imaging. *IEEE J. Sel. Top. Quantum Electron.* **2017**, *23*, 394–403.

(39) Sonneveld, M. J.; Zoutendijk, R.; Janssen, H. L. A. Hepatitis B Surface Antigen Monitoring and Management of Chronic Hepatitis B. *J. Viral Hepatitis* **2011**, *18*, 449–457.

(40) Galbiati, S.; Damin, F.; Pinzani, P.; Mancini, I.; Vinci, S.; Chiari, M.; Orlando, C.; Cremonesi, L.; Ferrari, M. A New Microarray Substrate for Ultra-Sensitive Genotyping of KRAS and BRAF Gene Variants in Colorectal Cancer. *PLoS One* **2013**, *8*, e59939.

(41) Zhang, X.; Servos, M. R.; Liu, J. Instantaneous and Quantitative Functionalization of Gold Nanoparticles with Thiolated DNA Using a

PH-Assisted and Surfactant-Free Route. *J. Am. Chem. Soc.* **2012**, *134*, 7266–7269.

(42) Edelstein, A. D.; Tsuchida, M. A.; Amodaj, N.; Pinkard, H.; Vale, R. D.; Stuurman, N. Advanced Methods of Microscope Control Using MManager Software. *J. Biol. Meth.* **2014**, *1*, 10.